Nanotextured surfaces for anti-icing

Michael Grizen[1], Tanmoy Maitra[1], Manish K. Tiwari[1,*]

*Corresponding author: Tel.: +44 (0)20131 081056; Email: m.tiwari@ucl.ac.uk
[1]Nanoengineered Systems Laboratory, UCL Mechanical Engineering, University College London,
Torrington Place, London WC1E 7JE, London, UK

ABSTRACT

Unwanted ice formation on surfaces is ubiquitous and often leads to catastrophic events, resulting in economic loss and costing human lives. Superhydrophobic nanotextured surfaces can circumvent such surface icing events either by minimizing the contact time between supercooled metastable liquid and surface or by suppressing ice nucleation events. However, such surfaces may not effectively inhibit icing under certain conditions. For example, superhydrophobic surfaces lose their non-wetting property when exposed to dynamically impacting water droplet/jet beyond a certain threshold velocity. Also, under high humidity conditions, surfaces become ineffective due to the formation of a frost layer. It has been shown that the roughness and thermal conductivity of the surface play a vital role to overcome aforementioned problems. In fact, substrate with high thermal conductivity (e.g. metals) can avoid the formation of the frost layer under. On the other hand, surfaces with precisely controlled nanotextures are beneficial to achieve high drop/jet impalement stability. With this perspective, we fabricated textured surfaces on aluminium, which has a plethora of industrial applications due to its high thermal conductivity and abundance in nature. Using a combination of wet etching and electrochemical approaches three kinds of micro/nano hierarchical surfaces were manufactured. Next, the surfaces were coated with fluorosilane to render them hydrophobic. We evaluated droplet/water-jet meniscus stability of the resulting surfaces, and discussed the role of different kinds of nanotextures on the impalement resistance of the surface.

KEY WORDS: Anti-icing, Nanotexture, Anodization, Frosting, Drop Impact, Jet impingement, Impalement Resistance

1. INTRODUCTION

Icing on infrastructures, such as bridges, wind turbines, airplanes wings is a common sight and, often, undesirable and harmful [1]. For instance, excessive accumulation of ice may cause structural failures as a result of increased mechanical loads[1]. Furthermore, icing on aircrafts reduces the smooth air-flow leading to increased air-drag. Icing is typically avoided by active thermal control systems, which, however, consume an additional energy and reduce overall system efficiency[1]. Therefore, the development of passive anti-icing strategy is of immense practical importance. In this regard, engineering of surfaces at the micro- and nanoscale can facilitate easier removal of ice, and can suppress ice formation [2,3]. In fact, nanotextured superhydrophobic surfaces that exhibit water drop contact angles >150° and roll off angles ~10° can repel metastable water droplets even down to ~ -18°C before freezing [4]. However, nanotextured superhydrophobic surfaces lose their non-wetting property when exposed to dynamically impacting water drops beyond a certain threshold velocity, rendering the surface ineffective[5–7]. Surface roughness plays an important role in repelling impacting droplets [7–9]. In fact, Checco *et al.* demonstrated surfaces with nanoscale roughness resisting impalement by millimetre-size drops up to speeds of 10 m/s [8]. In another work, carbon black nanoparticles/graphene nanoplatelets and a hydrophobic polymer composite exhibited resistance toward impacting droplets up to a speed of 5 m/s[10]. However, such nanotextured superhydrophobic surfaces become ineffective against repelling supercooled metastable water droplets due to the accumulation of frost, which is unavoidable under humid conditions [11,12]. In low humidity conditions, thermal conductivity plays an especially important role in freezing of supercooled droplets. A supercooled droplet on a surface is in a metastable state and will freeze if given enough time [13]. Droplet freezing starts with a fast (~10 ms),

kinetically controlled, recalescent stage, which freezes part of the liquid and releases heat of freezing [14]. This heat can be absorbed by the liquid part remaining in the droplet, leading to its evaporation and formation of a vapour halo around the freezing drop, as was studied in details in [11]. The vapour from the drop, however, must condense back down – due to low ambient temperature – and form a ring like frost layer around the mother droplet. This frozen ring can touch any neighboring droplets, e.g., when freezing is taking place through liquid droplets formed on a cold substrate. The size of the frozen ring is related to the thermal conductivity of the substrate on which a drop rests; in fact, highly conductive substrates such metals eliminate the formation of the frost ring [11]. This clearly highlights the benefit of high substrate thermal conductivity in anti-icing. Additionally, in a number of thermal applications such as refrigeration systems, ice-build up impairs the thermal performance. Thus, surfaces with shallow textures and, therefore, minimal thermal resistance should have a clear advantage in these applications.With this perspective, the current work is focused on surface manufacture and assessing the surface properties to ensure its fruitful potential applications in anti-icing, where, as argued above, thermal conductivity of the substrate plays an important role [11]. Therefore we seek to demonstrate the feasibility of aluminum based nanotextured superhydrophobic surfaces, where the surface texturing is deliberately controlled to remain shallow to limit the thermal resistance, while simultaneously ensuring the good features for anti-icing such as controlled texture (for freezing delay) [13], ability to resist droplet/liquid impalement for supercooled droplet impacts [4,7], and low adhesion of ice due to reduced receding contact angle [15]. Furthermore, those fabricated micro/nanotextured surfaces can be used in a number of positive applications in a wide verities of phase change processes, apart from surface icing, where surface roughness play a vital role. For example, optimizing/controlling boiling to facilitate nucleate boiling rather than film boiling which can enhance several times the heat transfer coefficient [16]; optimizing surfaces to promote highly efficient dropwise condensation over filmwise condensation [17]. Here, we follow scalable fabrication methods to control surface textures at micro/nano-scale on aluminum substrates, a widely used material in industry. We use aluminum as the substrate material and engineer it using scalable wet-chemical etching to fabricate shallow, step-like microtextures. Thereafter, two different techniques were used to create nano-scale morphologies on the microtextures, i.e., to obtain hierarchical roughness. The first technique was anodization [18], which led to nanoporous (np) or nanofiber (nf) structures. The second method was treating the surfaces in boiling water that resulted wrinkle like nanotextures (nw). The resulting micro/nano-hierarchical textures were designated by μ_{np}, μ_{nf} and μ_{nw} symbols, where μ denotes microstructure. Finally, all micro/nano- hierarchical surfaces were coated with fluorosilane to render them hydrophobic. We evaluated the stability of these surfaces using free-falling droplet, and water-jet impacts tests. Furthermore, we also performed stability tests on the nf surfaces alone, without underlying μ. The stability of other two nanostructures, nf and nw, however, were not studied since they did not show the superhydrophobic property without underlying microstructures. Lastly, we studied mechanical durability of micro/nano-hierarchical surfaces using a high tack tape peel test [19].

2. EXPERIMENTAL METHODS

2.1 Surface and chemicals Aluminum sheets with purity of 99.99%, working substrate in our study, was purchased from Alfa-Aesar. Acetone, isopropyl alcohol, n-hexane, oxalic acid, phosphoric acid, hydrochloric acid (HCl), and 1H,1H,2H,2H-Perfluorodecyltrichlorosilane (FDTS) $C_{10}H_4Cl_3F_{17}Si$ were purchased from Sigma Aldrich, and were used without further purification. Palladium Chloride ($PdCl_2$, reagent grade), and sodium hydroxide pellets (<98%, anhydrous) were also purchased from Sigma Aldrich.

2.2 Surface preparation The aluminum substrates (size 2 cm x 2 cm) were cleaned in acetone, isopropyl alcohol, and deionized (DI) water for 10 minutes each. To remove native oxide layer, the substrates were then treated in 1 wt.-% sodium hydroxide solution, and subsequently cleaned in DI water. To create step-like microstructures, aluminum substrates were etched in 0.6 (M) PdCl2/HCl solution for 5 minutes, followed by cleaning in DI water for 2-3 minutes. The representative scanning electron microscope (SEM) image of the microtextured substrate is shown in Fig. 1A. To fabricate micro/nano-hierarchical textures, we followed two different processes that result three kinds of nanostructures. A brief description of each process follows.
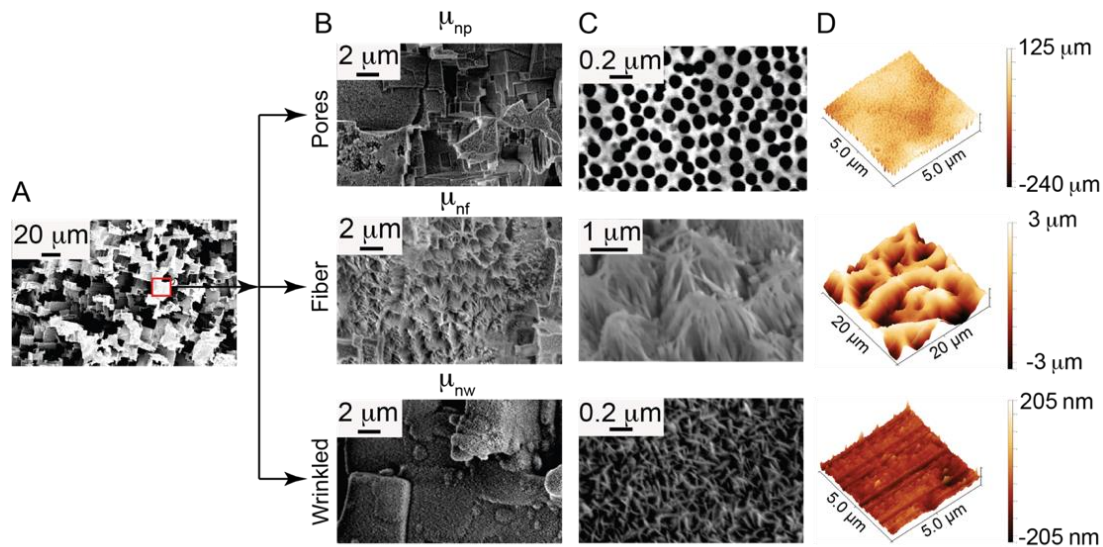
Fig. 1 Scanning electron microscopic (SEM) and atomic force microscopic (AFM) images of micro-, and micro/nano-hierarchical surfaces: (A) SEM image of step-like microtextures on aluminum, (B), (C) and (D) low- and high-resolution SEM images, and three-dimensional (3D) AFM images of three different nanotextures on microtextures; resulting hierarchical textures designated as μ_{np}, μ_{nf}, and μ_{nw}, respectively (np, nf and nw denote nanopores, nanofibers and nanowrinkle).

Anodization/ wet etching. To obtain nanoporous and nanofiber structures, anodization followed by a wet etching process was employed. A 0.3 (M) aqueous solution of oxalic acid was used as the electrolyte. Microtextured aluminum substrate and platinum (Pt) served as the anode and the cathode, respectively. After anodization, an array of well-ordered aluminum oxide nanotubes with thick pore walls was obtained. The pore wall thickness was thereafter gradually reduced by increasing the duration of etching time in 5 wt.-% phosphoric acid solution. Reducing pore wall thickness results in reduced solid fraction. Importantly, the lesser the solid fraction the higher the receding contact angles. Higher receding contact angles offer a number of advantages in anti-icing strategies, such as lowering ice adhesion strength [15], reducing metastable water droplet/surface contact time [7], and delay in freezing of water droplets [7]. Therefore, we optimized the pore widening time to obtain thin walled nanotubes, just before they collapsed to form nanofiber networks. The nanofibers networks, interestingly, also showed a low solid fraction resulting a high receding contact angle. The high-resolution SEM images in Fig. 1B and C shows the topology of the nanotube array. An additional etching for ~60 minutes resulted in a complete collapse of pore walls leading to the formation of a random fiber network (μ_{nf}), as shown in Fig. 1B and C. Similar anodization and pore widening on the polished smooth aluminum surfaces[20] to obtain nanopore (np), and nanofiber (nf) morphology.

Boiling water treatment. Microtextured aluminum foils were treated in boiling water for ~30 minutes to obtain wrinkled shaped nanostructures (μ_{nw}), as shown in Fig. 1B and C.

Lastly, all micro/nano-hierachical (μ_{np}, μ_{nf} and μ_{nw}), nf and nw surfaces were coated with 1.43 (M) solution of 1H,1H,2H,2H-Perfluorodecyltrichlorosilane in hexane for 2 hours, followed by baking at 110° C for 45 minutes. Microtextured aluminum (μ), without any nanotextures, and smooth (s, electrochemically/chemically polished) aluminum surface were also functionalized in the fluorosilane/hexane solution.
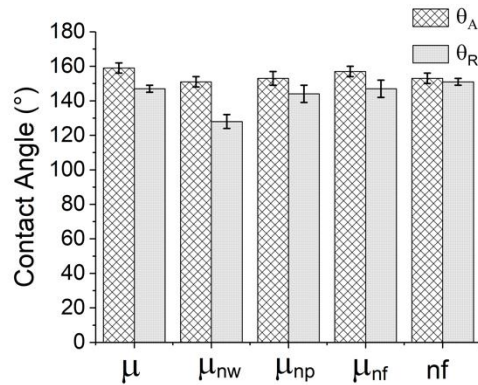
Fig. 2 Advancing (θ_A) and Receding (θ_R) water contact angles measured on μ, μ_{np}, μ_{nf}, and μ_{nw} surfaces.

2.3 Contact angle measurements An in-house goniometer system was used to measure advancing and receding contact angles of all micro/nano-hierarchical and nanotextured surfaces[7].

2.4 Free-falling water droplet impact test ~2.5 mm water droplets generated using a needle fitted to a syringe pump (PHD Ultra, Harvard Apparatus) were used. The highest drop speed attained was ~2.7 m/s, with a drop fall height of 45 cm. Beyond this height, the precise location of drop impact varied (due to air drag and gentle laboratory perturbations), making it difficult to fit the impact event in the imaging field of view. Each droplet impact was recorded with a high-speed camera (Phantom V411) at 10,000 frames per second.

2.5 Water jet impingement study The setup for jet impact tests is was similar to that described elsewhere [21]. Briefly, water jet was generated using a needle of internal diameter of 0.5 mm, connected to a nitrogen gas cylinder. The nitrogen pressure was regulated to vary the jet velocity. After the test, to evaluate whether liquid impalement on the surface, a ~7 µl water drop was placed at the area of surfaces exposed to the jet. An easy drop roll-off established the lack of impalement.
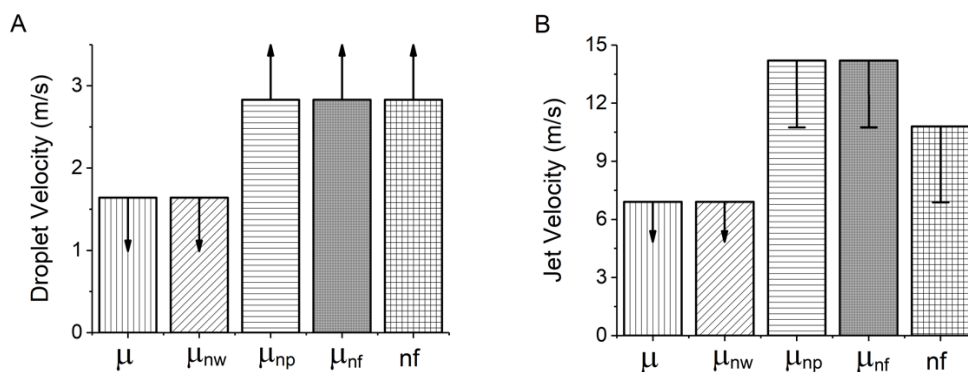

Fig. 3 Free-falling water droplet and jet impact experiments on μ, μ_{nw}, μ_{np}, μ_{nf}, and nf surfaces: (A) and (B) plot of threshold droplet impact velocities in free-falling drop impact and jet impingement experiments. μ and μ_{nw} show impalement even at the minimum impact velocities of 1.5 m/s for drop and 6.25 m/s jet impact test, in our experimental setup. This indicates a lower threshold of impalement on these surface (marked by downward arrows). μ_{np}, μ_{nf}, and nf surfaces do not show impalement even up to maximum drop impact speed in our setup (marked by upward arrows). The error bars in (B) indicate the uncertainties of nitrogen pressure regulator (0.5 bar). The bar heights in (B) indicate the threshold impact speed at which 40% of the impacts led to impalement and the half error bars mark the minimal speed at which impalement was observed at all.

2.6 Mechanical durability test The tape peel test was performed using a high tack 3M VHB^{TM} tape. Advancing and receding contact angles were measured after every 10 cycles of tape peel test.

3. Discussions

The SEM and AFM images of μ_{np}, μ_{nf} and μ_{nw} are presented in the Fig. 1D.

Fig. **2** shows the advancing (θ_A) and receding (θ_R) contact angles of μ, μ_{np}, μ_{nf}, μ_{nw} and nf surfaces. θ_A and θ_R of all surfaces are higher than 150° and 140°, respectively. The wetting characteristics are closely linked to the surface anti-icing behavior. For example, an increase in the θ_A improves the liquid impalement resistance, which enables better resistance to freezing via supercooled droplet impacts [4,7]. On the other hand, an increase in θ_R wangles lower ice-adhesion [15].

The low hysteresis (difference of θ_A and θ_R) indicates the drops attaining a Cassie state on these surfaces. The solid fraction of such random micro- and nano- surfaces, with different elevations, cannot be estimated by considering either geometry or analysis of SEM images. Therefore, we estimated surface solid fractions (ϕ) by employing the Cassie equation [7]

$$\cos \theta_A = -1 + \phi(1 + \cos \theta_A^*) \tag{2}$$

where θ_A^* denotes Young's contact angle on the smooth functionalized aluminum surface (s) that was measured to be 103±3°. The resulting ϕ of μ (ϕ_μ) and nf (ϕ_{nf}) surfaces turned out to be 0.16 and 0.07, respectively. For the μ_{nf} surface, ϕ is the product of ϕ_μ and ϕ_{nf}, which is estimated to be 0.063. A slight lower value ϕ for μ_{nf} compared to nf alone is attributed to the length of nanofibers, which is shorter on the microtextured aluminum (
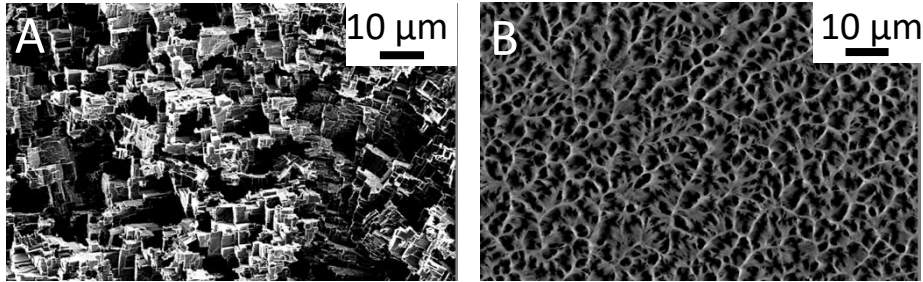Fig. **4**A) compared to the smooth aluminum (
Fig. **4**B).

Fig. 4 SEM image of (A) μ_{nf} and (B) nf surfaces at same magnification. Nanofibers are clearly visible only in (B), indicating that the lengths of nanofibers are relatively large on the smooth compared to that of the microtextured aluminium surface.

The stability of surfaces against free-falling water droplet were studied first; the results are presented in the Fig. **3**A. To ensure reproducibility, droplet impact experiments were done on 3-4 different locations on surfaces from two different fabrication batches. The drop falling height was altered at an interval of 15 cm, from 15 cm up to 45 cm. μ and μ_{nw} showed impalement at a velocity of ~1.5 m/s. The corresponding Weber number (We) – defined as $\left(\rho V^2 D / \gamma\right)$, i.e. ratio of inertia and capillary forces [7,22], with the symbols ρ and γ denoting the liquid density and surface tension, V the velocity and the D the drop or jet diameter – is ~ 130. μ_{np}, μ_{nf}, and nf surfaces did not show impalement up to ~2.7 m/s, i.e., the maximum drop speed in our setup.
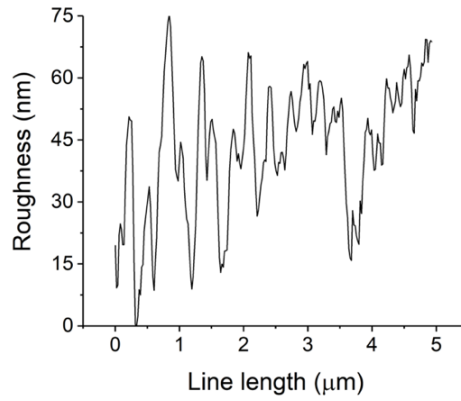
Fig. 5 Profile from an AFM scan on nw surface, used to estimate the width and height of the nanostructures.

Next, we performed the jet impact test on the surfaces, the corresponding results are summarized in Fig. **3**B. Jet impact speed was varied by altering nitrogen back pressure, in increments of 0.5 bar. μ and $μ_{nw}$ showed impalement at the velocity of 6.25 m/s, the minimum jet speed in our setup. Impressively, $μ_{nf}$ and $μ_{np}$ resist a jets speeds of 14 m/s, corresponding $We\sim$ 1350. The nf surface also showed a high impalement resistance, resisting jets with speeds of 11 m/s ($We\sim$ 840), which is consistent with the previous study on the similar nanofiber structures [23]. Note that, the previous study[23] showed that similar nanofiber structures on a smooth aluminum surface can repel impact of 2-mm sized water drops up to $We\sim$3000. However, the surfaces were not tested with jet impact, which offers a more severe test of durability.

One of the strengths of our chemical and electrochemical etching for micro, nano and hierarchical texture is the ability to alter the surface manufacturing parameters and precise control of the morphology, which is directly related to the capillary pressure. The impact resistance of textured surfaces can be quantified by capillary pressure (P_c). P_c for random micro and nanotextures can be expressed as[24]

$$P_C = f(\theta_A^*, \gamma, \phi, d, a) \tag{3}$$

where γ, d and a denote the liquid/air surface tension, the gap between the roughness asperities, and the size of the asperities, respectively. For example, for nf surface, a and d refer to diameter of nanofibers and gap between nanofibers, respectively. If γ, ϕ and a remain constant, then P_C scales as $1/d$. For the μ surface, step-sizes (a) are ~10 µm, and d ~20 µm (refer to the SEM image in Fig. 1A), resulting in a capillary pressure ~ 3.6 kPa (taking γ as 0.072 N/m). The relatively low value of P_C results in easy ipalement of the surface by liquid meniscus even at minimal tested impact speeds and leads to the loss of superhydrophobic property. The nanotextures nw, ns and nf (each with $d\sim$ 100 nm) were imparted on these microtextures to improve impalement resistance. The low droplet impact resistance on $μ_{nw}$ surfaces, however, clearly shows no improvement. This can be rationalized by appreciating the shallowness of nw textures that may facilitate easy touchdown[22] of water meniscus to the bottom of the asperities. This can be verified by considering scaling analysis based on the geometry of nw textures. Additionally, since both μ and $μ_{nw}$ surfaces show meniscus impalement at the same impact drop and water-jet impact velocity, it can be assumed that both have P_C in the same order of magnitude i.e. ~3 kPa. The critical impalement pressure for touchdown scenario $\left(P^{imp}\right)$ scales as $\sim\left(\frac{h}{r^2}\right)\gamma$[22], where h and r denote height and width of the wrinkle features in nw. The values of h and r both are estimated from the AFM line scan (see in Fig. 5) as ~50 nm and 400 nm, respectively. This results in P^{imp} turns out to be ~10 kPa, which is in the same order of magnitude as the P_C. Therefore, touchdown mechanism is plausible for the nw nanostructures.

The result indicates that the aspect ratio of nanotextures $\left(h/r\right)$ should be increased to overcome the meniscus touchdown and improve the impalement resistance. Indeed, our results show $μ_{np}$, $μ_{nf}$, and nf, which all have high-aspect ratios, also demonstrate impressive impact resistance. Interestingly, surfaces with np texture alone,

without microtextures, did not show superhydrophobic property, possibly due to a high $\phi \sim 0.22$, as estimated from Eq. (2) and considering θ_A for np surface to be $147\pm3°$. The beneficial role of nanoporous structure is only realized when it is introduced on microtextures that reduce the ϕ. μ_{np} are performing equally good as μ_{nf}. However, introducing nf on μ slightly improves the impact resistance compared to the nf surface alone. This can be explained by considering the ϕ value of these surfaces: $\phi_{\mu_{nf}}$ is slightly lower than ϕ_{nf}, and the lower ϕ facilitates an easier recovery of the impaled water meniscus due to entrapped air layer in nanofibers. The recovery mechanism was reported earlier by Verho et al. on similar nanotextures [19].

One of the strengths of our employed chemical and electrochemical etching techniques is the ability to precisely control of the morphology, which is directly related to the capillary pressure. Importantly, the wetting characteristics are closely linked to the surface anti-icing behavior. For example, an increase in the θ_A improves the liquid impalement resistance, which enables better resistance to freezing via supercooled droplet impacts [4,7]. On the other hand, an increase in θ_R enables lower ice-adhesion [15].

With the μ_{nf} surface showing the best impalement resistance, we also tested it using tape peel test. θ_A and θ_R were measured after every 10 tape peel cycles (Fig. 6). The results indicates that the surfaces retains its superhydrophobic property after 50 cycles; this is consistent with [19], where this robustness of FDTS was first reported documented.
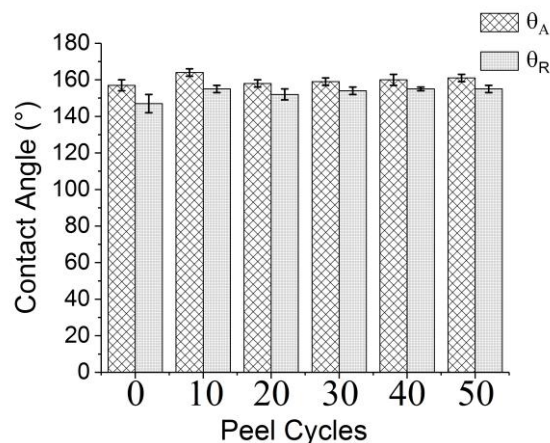

Fig. 6 Effect of tape peel tests on wettability of the μ_{nf} surface.

4. Conclusion

We followed a scalable surface manufacturing process on aluminium to control surface roughness at micro- and nanoscale. The surfaces were assessed using water droplet and jet impact tests. Micro/nano-hierarchical surfaces with nanofibers and nanopores showed excellent droplet and jet impalement resistance, resisting jets up to a velocity of 14 m/s. We discussed the role of micro- and different nanostructures on deciding impalement resistance and the maximal impact speeds on our surfaces. Our results identify two crucial roles of nanotextures to obtain high speed liquid impalement resistance: providing a high capillary resistance due to nanoscale roughness asperities, and exploiting the rationally conceived nanotextures to facilitate an easy recovery of impaled water meniscus out of the microtexture in a hierarchically roughness surfaces.

5. Acknowledgement

REFERENCES

[1] Civil Aviation Authority, Aircraft icing Handbook, Safety Education and Publishing Unit, Civil Aviation Authority, Lower Hutt, New Zealand, 2000.

[2] J. Lv, Y. Song, L. Jiang, J. Wang, Bio-Inspired Strategies for Anti-Icing, ACS Nano. 8 (2014) 3152–3169. doi:10.1021/nn406522n.

[3] T.M. Schutzius, S. Jung, T. Maitra, P. Eberle, C. Antonini, C. Stamatopoulos, D. Poulikakos, Physics of Icing and Rational Design of Surfaces with Extraordinary Icephobicity, Langmuir. 31 (2015) 4807–4821. doi:10.1021/la502586a.

[4] T. Maitra, C. Antonini, M.K. Tiwari, A. Mularczyk, Z. Imeri, P. Schoch, D. Poulikakos, Supercooled Water Drops Impacting Superhydrophobic Textures, Langmuir. 30 (2014) 10855–10861. doi:10.1021/la502675a.

[5] M. McCarthy, K. Gerasopoulos, R. Enright, J.N. Culver, R. Ghodssi, E.N. Wang, Biotemplated hierarchical surfaces and the role of dual length scales on the repellency of impacting droplets, Appl. Phys. Lett. 100 (2012) 263701. doi:10.1063/1.4729935.

[6] P. Hao, C. Lv, F. Niu, Y. Yu, Water droplet impact on superhydrophobic surfaces with microstructures and hierarchical roughness, Sci. China Physics, Mech. Astron. 57 (2014) 1376–1381. doi:10.1007/s11433-014-5472-7.

[7] T. Maitra, M.K. Tiwari, C. Antonini, P. Schoch, S. Jung, P. Eberle, D. Poulikakos, On the Nanoengineering of Superhydrophobic and Impalement Resistant Surface Textures below the Freezing Temperature, Nano Lett. 14 (2014) 172–182. doi:10.1021/nl4037092.

[8] A. Checco, A. Rahman, C.T. Black, Robust Superhydrophobicity in Large-Area Nanostructured Surfaces Defined by Block-Copolymer Self Assembly, Adv. Mater. 26 (2014) 886–891. doi:10.1002/adma.201304006.

[9] S. Jung, M. Dorrestijn, D. Raps, A. Das, C.M. Megaridis, D. Poulikakos, Are Superhydrophobic Surfaces Best for Icephobicity?, Langmuir. 27 (2011) 3059–3066. doi:10.1021/la104762g.

[10] A. Asthana, T. Maitra, R. Büchel, M.K. Tiwari, D. Poulikakos, Multifunctional Superhydrophobic Polymer/Carbon Nanocomposites: Graphene, Carbon Nanotubes, or Carbon Black?, ACS Appl. Mater. Interfaces. 6 (2014) 8859–8867. doi:10.1021/am501649w.

[11] S. Jung, M.K. Tiwari, D. Poulikakos, Frost halos from supercooled water droplets., Proc. Natl. Acad. Sci. U. S. A. 109 (2012) 16073–8. doi:10.1073/pnas.1206121109.

[12] S. Jung, M.K. Tiwari, N.V. Doan, D. Poulikakos, Mechanism of supercooled droplet freezing on surfaces, Nat. Commun. 3 (2012) 615. doi:10.1038/ncomms1630.

[13] P. Eberle, M.K. Tiwari, T. Maitra, D. Poulikakos, Rational nanostructuring of surfaces for extraordinary icephobicity, Nanoscale. 6 (2014) 4874–81. doi:10.1039/c3nr06644d.

[14] A. Criscione, I. V. Roisman, S. Jakirlić, C. Tropea, Mechanism of supercooled droplet freezing on surfaces, Int. J. Therm. Sci. 92 (2015) 150–161. doi:10.1038/ncomms1630.

[15] A.J. Meuler, J.D. Smith, K.K. Varanasi, J.M. Mabry, G.H. McKinley, R.E. Cohen, Relationships between water wettability and ice adhesion, ACS Appl. Mater. Interfaces. 2 (2010) 3100–3110. doi:10.1021/am1006035.

[16] D. Attinger, C. Frankiewicz, A.R. Betz, T.M. Schutzius, R. Ganguly, A. Das, C.-J. Kim, C.M. Megaridis, Surface engineering for phase change heat transfer: A review, MRS Energy Sustain. 1 (2014) E4. doi:10.1557/mre.2014.9.

[17] D. Torresin, M.K. Tiwari, D. Del Col, D. Poulikakos, Flow condensation on copper-based nanotextured superhydrophobic surfaces, Langmuir. 29 (2013) 840–848. doi:10.1021/la304389s.

[18] T. Kikuchi, O. Nishinaga, D. Nakajima, J. Kawashima, S. Natsui, N. Sakaguchi, R.O. Suzuki, Ultra-High Density Single Nanometer-Scale Anodic Alumina Nanofibers Fabricated by Pyrophosphoric Acid Anodizing, Sci. Rep. 4 (2015) 7411. doi:10.1038/srep07411.

[19] T. Maitra, C. Antonini, M. Auf der Mauer, C. Stamatopoulos, M.K. Tiwari, D. Poulikakos, Hierarchically nanotextured surfaces maintaining superhydrophobicity under severely adverse conditions, Nanoscale. 6 (2014) 8710–8719. doi:10.1039/C4NR01368A.

[20] K.M. Alam, A.P. Singh, S.C. Bodepudi, S. Pramanik, Fabrication of hexagonally ordered nanopores in anodic alumina: An alternative pretreatment, Surf. Sci. 605 (2011) 441–449. doi:10.1016/j.susc.2010.11.015.

[21] H. Sojoudi, M. Wang, N.D. Boscher, G.H. McKinley, K.K. Gleason, Durable and scalable icephobic surfaces: similarities and distinctions from superhydrophobic surfaces, Soft Matter. 12 (2016) 1938–1963. doi:10.1039/C5SM02295A.

[22] D. Bartolo, F. Bouamrirene, É. Verneuil, A. Buguin, P. Silberzan, S. Moulinet, Bouncing or sticky droplets: Impalement transitions on superhydrophobic micropatterned surfaces, Europhys. Lett. 74 (2006) 299–305. doi:10.1209/epl/i2005-10522-3.

[23] T. Maitra, S. Jung, M.E. Giger, V. Kandrical, T. Ruesch, D. Poulikakos, Superhydrophobicity vs. Ice Adhesion: The Quandary of Robust Icephobic Surface Design, Adv. Mater. Interfaces. 2 (2015) 1500330. doi:10.1002/admi.201500330.

[24] S. Dash, M.T. Alt, S. V. Garimella, Hybrid Surface Design for Robust Superhydrophobicity, Langmuir. 28 (2012) 9606–9615. doi:10.1021/la301743p.